



Comparison between object and image plane cross-correlation for stereoscopic PIV in the presence of pixel locking

Girish K. Jankee¹ · Bharathram Ganapathisubramani¹

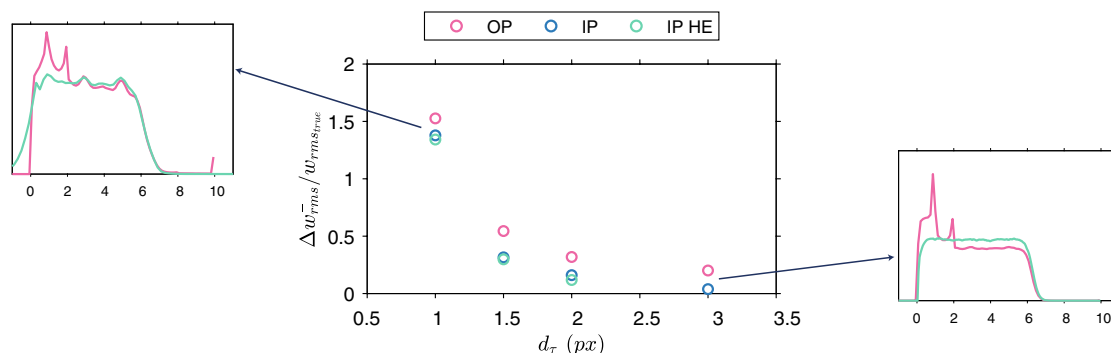
Received: 27 August 2019 / Revised: 28 November 2019 / Accepted: 11 February 2020
 © The Author(s) 2020

Abstract

Pixel locking in stereoscopic particle image velocimetry (SPIV) is often overlooked, albeit the existence of studies demonstrating an influence on turbulent statistics. Such a bias error occurs when the seeding particles have an image diameter in the range of 1–2 pixels. Together with the advent of superior cameras and more powerful lasers, new image-processing techniques enable large field of views to be examined. Under such circumstances, defocusing is not an option and due to the small nature of the particle image diameter, pixel locking is inherent in the data. This study analyses the contrast between object plane-based and image plane-based approach for cross-correlation in the presence of pixel locking in SPIV. By combining experimental data and synthetic images, the sensitivity of pixel locking on single-point statistics is quantified and a protocol is proposed to tackle such an increasingly prevalent condition. A consequence of pixel locking is the occurrence of Moiré fringes, whose intensity is observed to be enhanced in the presence of particles with an image diameter less than 2 pixels. Such high frequency artifacts are not only receptive to the fill factor of the sensor but also depend on the residual error of the interpolation from image plane to the object plane. This study discusses the origins of Moiré fringes in SPIV and provides a method to mitigate these based on the type of cross-correlation used.

Graphic abstract

Variation of the difference in RMS between the true value and the derived value from diverse adopted methodologies as the particle image diameter, d_τ increases. (OP: Object plane cross-correlation, IP: Image plane cross-correlation, IP HE: Image plane cross-correlation post histogram equalisation)



1 Introduction

Over the past decades, the evolution of PIV as a state-of-the-art measurement technique has been accompanied by a need to quantify and curtail its associated uncertainty. The accuracy of a PIV system has been found to be sensitive to properties of the flowfield, the seeding density, the optical set-up as well as the data acquisition and

✉ Girish K. Jankee
 G.Jankee@soton.ac.uk
 Bharathram Ganapathisubramani
 G.Bharath@soton.ac.uk

¹ Aerodynamics and Flight Mechanics, Faculty of Engineering and Physical Sciences, University of Southampton, Southampton SO17 1BJ, UK

processing methodology (Chen and Katz 2005). In general, the uncertainty can be classified as either random or biased. Random errors minimally influence the accuracy of measurements, provided a large ensemble dataset is used (Christensen 2004). However, such an approach is not germane to bias errors, such as pixel locking, which remain ingrained in imaging techniques.

Pixel locking has been extensively investigated for planar PIV systems and involves particle displacements being biased towards integer values (Westerweel 1997). Such characteristic has been consistently observed during the estimation of sub-pixel disparity. The process comprises fitting n -order polynomials through a few points found in proximity of discrete correlation peaks. In the presence of pixel locking, the sub-pixel disparity has been found to shift towards integer values (Chen and Katz 2005; Raffel et al. 2007; Adrian and Westerweel 2011). There exists a number of reasons to explain the occurrence of pixel locking. Christensen (2004) highlighted the choice of sub-pixel estimator and the under-resolved sampling of particle images. Fore (2010) found pixel locking to be inherent if during sub-pixel interpolation, the correlation function away from the peak is greater than zero, thus underlining the unwarranted assumption that the correlation peak can always be approximated using a Gaussian function. Hearst and Ganapathisubramani (2015) described pixel locking as an intrinsic error imbedded in the images at the time of acquisition and attributed its presence to insufficient resolution of the datasets. Adrian and Westerweel (2011) found pixel locking to be dependent on the size of the image particle diameter and established an optimal threshold of two pixels beyond which pixel-locking effects are mitigated. Michaelis et al. (2016) also corroborated these findings and reported a range of 2–4 pixels in order to avoid pixel locking.

The presence of pixel locking potentially leads to misguided interpretation of properties of turbulent flows. Christensen (2004) found that all flow statistics, besides the mean velocity, were influenced by pixel locking. This highlights the significance of such a bias error engendering flawed analysis as in the case of flows with uniform momentum zones (UMZs). For example, direct numerical simulations (DNS) of a fully developed channel flow found that UMZs contained no bias towards particular velocity values, thus contradicting the experimental PIV data from Kwon et al. (2014) which showed the presence of modal velocities under same flow conditions. Such discrepancy can be attributed to pixel-locked data in the experimental case. Another subtle phenomenon arising from pixel-locked data is the occurrence of artifacts or patterns termed as Moiré fringes.

The appearance of such fringes is commonly attributed to the interference between the spacing in the camera sensor array and any length scale related to the physical elements being recorded (Wen and Khatibi 2015). Aliasing which

involves undersampling of light is a potential cause of Moiré fringes and is dependent on the fill factor of the sensor. The fill factor represents the portion of the total area of a pixel which is sensitive to the incident photons. Higher spatial and temporal quantum efficiency can be achieved by a larger fill factor. In a camera sensor, aliasing is usually avoided as the pixel window or the aperture acts as a low-pass filter which clears the image of any high frequency features. For low fill factor sensors, when Nyquist theorem is not satisfied, high frequencies which leak into the image can be observed as fringes or line patterns. In the context of PIV, the occurrence of Moiré fringes can also be attributed to askew calibration coefficients which results in substantial residuals during the interpolation between the image plane and the object plane (Fig. 1). The intensity of the fringes depends on the degree of pixel locking due to the correlation between the residual of the interpolation process and the particle image diameter. Although not asserted, such artifacts are visible in the pixel-locked data of Nogueira et al. (2009) and can be observed to reduce in intensity with pixel-locking treatment.

A key aspect when dealing with pixel locking is to avoid under-resolved sampling of PIV images. This has led to multiple studies contemplating contrasting schemes. A priori techniques include defocusing the camera image, the use of different lens apertures or incorporating diffuser plates between the lens and the camera sensor (Michaelis et al. 2016). Kislaya and Sciacchitano (2018) performed an in-depth analysis of the performance of diffusers and noted a reduction in both the systematic and random error by a factor of 3 when 2 diffusers were used. In comparison to image defocussing, which has constraints and is not effective for stereo- or tomo-PIV configurations, under conditions of low signal to noise ratio (SNR), Kislaya and Sciacchitano (2018) found no deterioration in the performance of diffusers.

Alternatively, improvement in the interpolation methods has been sought. Lecordier et al. (2001) used spectrum analysis to assess the accuracy of different interpolation schemes while Gui and Wereley (2002) observed an alleviating influence on pixel locking when the correlation-based algorithm involves continuous window-shifts rather than discrete window-shifts. Other approaches are related to anti pixel-locking filters (Michaelis et al. 2016). Fincham and Delerce (2000) segregated the error in imaging algorithms as either the root mean square (RMS) component or the pixel-locked component and affirmed that the two components can be treated independently. The RMS component of the sub-pixel error experienced substantial reduction when the local fluid deformation was incorporated into the correlation image velocity (CIV) algorithm. Further, a peak anti-aliasing spline transformed interrogation scheme (PASTIS) was developed and successfully treated the manifestation of the pixel-locked component of the error.

Roesgen (2003) defined a “sinc” function which uses nearest-neighbour interpolation with a top hat kernel. The attributes of such a method were observed to be limited attenuation of the pass-band data as well as efficient suppression of the interpolation-related part of the pixel-locking error. Chen and Katz (2005) developed the concept of correlation mapping method (CMM) which uses sub-pixel interpolation to express the second exposure of an interrogation window with a polynomial function where the displacement is unknown. The coefficients of this polynomial can be established via greyscale distribution of the first image. Hence, the correlation between this function and the first exposure is likewise a polynomial of the displacement. Finally, using a least squares method, the minimum difference between the real and virtual correlation yields the optimal displacement components. The advantage of such a technique, in comparison to smooth sub-pixel curve-fitting, is a reduction in both pixel-locking bias and the random error. Fore (2010) achieved reduction of the total and bias errors by employing the covariance function to uniformly distribute the random error across the sub-pixel displacement.

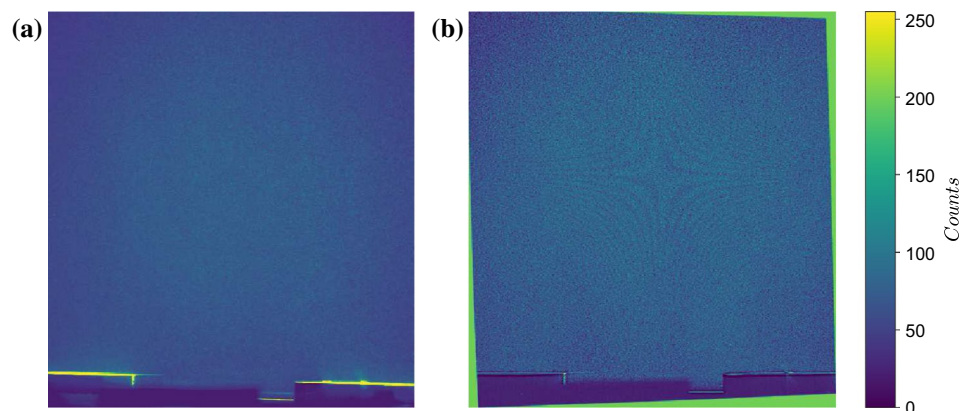
Roth and Katz (2001) used histogram equalisation as a post-processing tool to mitigate the effect of pixel locking. The concept incorporates mapping an uneven probability distribution onto an even distribution in order to improve the accuracy of the sub-pixel displacement around an integer value. Hearst and Ganapathisubramani (2015) applied the same method to quantify and adjust pixel locking. A quantification metric was computed by integrating the histogram-equalised transfer function and normalising with the worst-case scenario. In doing so, it was observed that pixel-locking is non-uniform across a vector field and hence, adjustments cannot be carried out uniformly across the field. Subsequently, a protocol was established where pixel-locking adjustment is selectively applied in an attempt to preserve non-integer peaks. Nogueira et al. (2009) proposed a novel method which used multiple Δt to estimate the magnitude of the pixel-locked error. The use of such a concept allow the real pixel displacement to be determined although its

application is limited as it requires the images to be recorded over a range of Δt and has been observed to be effective only for mean steady flows.

These precursory schemes work well for planar PIV systems. However, as highlighted by Hearst and Ganapathisubramani (2015), SPIV poses a peculiar problem. Beresh et al. (2016) explained that significant bias errors persist for large stereoscopic angles, thick laser sheets and small particle diameters following application of self-calibration techniques. Indeed, when processing multiple simultaneously-acquired images, pixel locking becomes locally more substantial in the processed vector fields. Since pixel-locking is intrinsic to individual frames, the reconstructed vector cannot undergo adjustments using the previously-described methods. For example, Hutchins et al. (2005) reported the presence of pixel locking and its influence on the RMS and Reynolds shear stress statistics in their SPIV calculations, despite the use of a Gaussian sub-pixel estimator. Such symptoms are increasingly prevalent in studies dealing with flows over rough surfaces or channel flows since away from the wall, the magnitude of the fluctuating displacement is less than 0.5 pixels and this exacerbates the error due to pixel-locking (Christensen 2004).

Although overlooked in the field of fluid mechanics, pixel locking has been subjected to research pertaining to stereo-vision in robotics and autonomous vehicles. Shimizu and Okutomi (2002) employed the sum of squared differences to estimate the sub-pixel displacement and found a reduction of up to 80% in the estimation error in comparison to conventional methods. Stein et al. (2006) proposed the use of adaptable affine windows, based on the concept of Lucas–Kanade tracking, in an attempt to predict the sub-pixel disparity estimates with increasing accuracy. By iteratively shifting and locally adapting the shape of the interrogation window, the Lucas–Kanade approach uses an initial integer disparity map to estimate the sub-pixel disparity. As opposed to standard parabola fitting, such a method has the potential to effectively reduce pixel locking. In spite of such progress, the circumscribed application of these methods to fluid mechanics signifies that pixel

Fig. 1 Appearance of Moiré fringes during the interpolation process from **a** image plane to **b** object plane under pixel-locked conditions, where the mean particle image diameter is less than 2 pixels



locking still remains an equivocal subject in the context of SPIV. A possible reason is the complexity in detecting pixel locking when using an object plane-based cross-correlation method for vector field reconstruction. Such a process involves sub-pixel interpolation in both dewarping the raw images and the multi-pass window deformation stages, which, in addition to degrading the image, also tend to neglect any contribution of the pixel locking bias since the latter is inherent in individual camera image frames.

Figure 2 epitomises such a situation where single-point statistics of a zero pressure gradient turbulent boundary layer are compared for a non-pixel-locked case (Case A) and its truncated variant (Case B). The latter represents a scenario of absolute pixel locking as the pixel displacements in both cameras have been rounded off to integer values. The histogram shown in Fig. 2a represents the pixel displacement in the left camera image and cannot be determined once the images have been dewarped as in the case of object plane-based cross-correlation. Hence, any presence of pixel locking is overlooked using that method and although, customary to the findings of Christensen (2004), the mean velocity profile remains unaffected, there is significant deviation in the RMS of the reconstructed component (Fig. 2b, c). The presence of pixel locking in the image plane in SPIV can be attributed to several factors which include the particle image diameter and the variation in magnification factor across the image. As underlined by Overmars et al. (2010), the particle image diameter, d_τ , holds particular significance in pixel locking and under conditions of in-focus particles, negligible lens aberrations and high enough f -stop values, it can be determined using the diameter of the tracer particles, d_p , the diffraction-limited spot diameter, d_s , the aperture number of the wavelength, $f^\#$, and the light wavelength, λ (Adrian and Westerweel 2011).

$$d_\tau \cong \sqrt{M_0^2 d_p^2 + d_s^2}, \quad (1)$$

where,

$$d_s = 2.44(M_0 + 1)f^\# \lambda. \quad (2)$$

Although in most cases, the tracer particles are diffracted-limited, Eqs. (1) and (2) stress that the magnification factor, M_0 , determines the dominant criterion between $M_0 d_p$ and d_s , thus influencing the performance of a PIV system. This is conspicuous in SPIV where the angle between the optical axes of the lens and the normal of the laser sheet contributes to a variation in the magnification factor across the image. Such situations are likely to be encountered in large field of view studies such as high speed SPIV, carried out with complementary metal-oxide-semiconductor (CMOS) cameras, where the pixels are large. Under these conditions, the measurements are subjected to a reduction in image magnification

leading to smaller image particle diameters, typically in the range of 1–2 pixels.

Since the uncertainty in SPIV is a combination of uncertainty associated with the pixel displacement in each camera image, object plane cross-correlation potentially results in erroneous vector fields if pixel locking is not treated for each camera individually. This study introduces a framework which uses image plane cross-correlation as a foundation to apply histogram equalisation on a vector-by-vector basis per image per camera prior to reconstruction of the 2D3C velocity field and application of any scaling parameters. The aim of adopting an approach which corrects for pixel-locking bias in the image plane is also expected to forestall the generation of Moiré fringes as this minimises the interpolation error which occurs when mapping from image to object plane. The proposed strategy is tested on synthetically generated SPIV images and validated through experimental data (Fig. 3).

2 Methodology

In an attempt to discern any influence of pixel locking on the velocity reconstruction procedure in SPIV, the acquired images are processed using both a commercial software and an in-house stereoscopic PIV reconstruction script. The fundamental difference between these two methods lies in the manner the cross-correlation is performed. While the commercial software dewarps the images first and computes fluidic displacements at the world grid positions (object plane-based cross-correlation), the in-house script computes 2D2C pixel displacements for the raw images in a grid in the image plane prior to 2D3C reconstruction with mapping and scaling to the object plane. Such an approach allows pixel-locking corrections to be locally applied in each camera frame.

In an attempt to illustrate the implementation of the methodology, the histogram equalisation procedure from Hearst and Ganapathisubramani (2015) is adopted in this paper, although it should be noted that there are various other pixel locking-correction techniques, as described in Sect. 1, which could be used. The reader is referred to the corresponding paper for an in-depth explanation of the protocol used in the quantification and adjustment of pixel locking. Following cross-correlation of consecutive frames for each camera independently, an initial assessment of the level of pixel locking is performed by generating histograms of the streamwise, u and wall-normal, v , particle displacement distributions in pixels. Hearst and Ganapathisubramani (2015) quantifies pixel locking by integrating the histogram equalised transfer function and normalising by the worst-case scenario. For each point in the vector field found to be contaminated by pixel-locking, a transfer function is generated

to reorganise the sub-pixel displacement histogram such that any bias towards a sub-pixel value of zero is eliminated.

The final stage consists of reconstructing the stereo velocity field with the data mapped and scaled to the object plane based on the calibration function and pixel-locking corrected histogram-equalised vector fields (Fig. 2). During this process, the resolution of the 2D3C field is kept identical to the vector field of the commercial software to ensure that the influence of the interpolation from the image plane to the world grid coordinates in the object plane is kept at a minimum and hence, an adequate comparison of the average resolution across the field can be carried out between the two methodologies used (Tables 1, 2).

3 SPIV setup

The predefined methodology was applied on experimental data and synthetic images, with the former having a streamwise SPIV configuration (Fig. 4) and the latter a cross-stream SPIV configuration. Data was acquired experimentally in the 3 × 2 ft suction wind tunnel facility at the University of Southampton. The 4 m long test section was filled with a repeatable roughness element spanning the entire width. Streamwise SPIV measurements were performed using two Lavision Imager Pro LX 16MP cameras, each fitted with a 300 mm *f*/8 Nikon lens and locked at an angle, θ corresponding to 35°, facing the region of interest (Fig. 4). A Litron 200 mJ dual pulse Nd-YAG laser is used to create a laser sheet with a thickness of 1 mm while seeding is provided by a Martin Magnum 1200 machine, ejecting particles with a mean physical diameter of 1 μm .

All the analysis presented in this study were computed by employing the following settings, unless otherwise specified. As part of image pre-processing, a sliding

background subtraction was applied to the raw images to reduce noise. The raw images were then processed with 4 passes of decreasing window size from 64 × 64 pixels to 24 × 24 pixels for stereo cross-correlation in the object plane and sequential cross-correlation for each camera in the image plane-based method. This resulted in a resolution of 1 vector per 0.1899 mm for the reconstructed 2D3C field in object plane while the average resolution of the pixel displacements for each camera in image plane was 1 vector every 6 pixels. It is not possible to directly compare the resolution at this stage as there is a variation in magnification across the camera image in image plane. However, the resolution of the 2D3C velocity field was maintained at 1 vector every 0.19 mm following the reconstruction phase, which enabled an adequate comparison between object plane and image plane-based cross-correlation.

4 In-house SPIV reconstruction

The in-house script applies a polynomial-based concept to back-project the apparent in-plane displacements in the object plane for each camera (Soloff et al. 1997). This involves combining planar cross-correlation results from the raw images for each camera and the dewarped vector locations in the object plane (Fig. 5).

The initial stage consists of evaluating the mapping functions (Eqs. 3–5) from the object plane (world units) to the image plane (pixels) using images of the calibration target and known locations of the marker coordinates.

$$X_{\text{left}} = f_1(x, y, z), \quad (3)$$

$$Y_{\text{left}} = f_2(x, y, z), \quad (4)$$

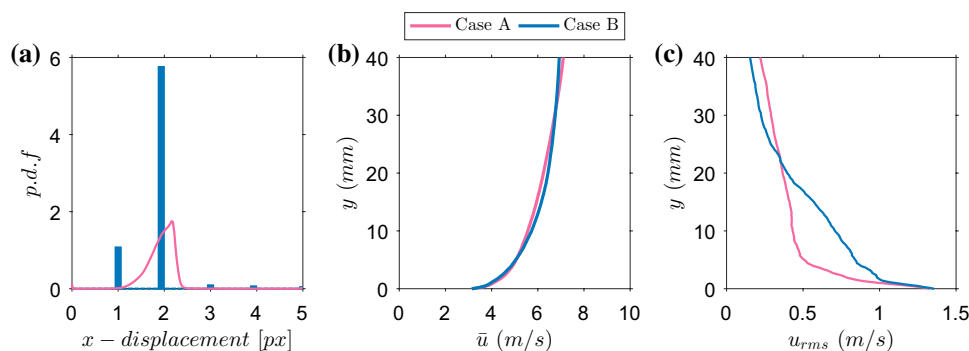
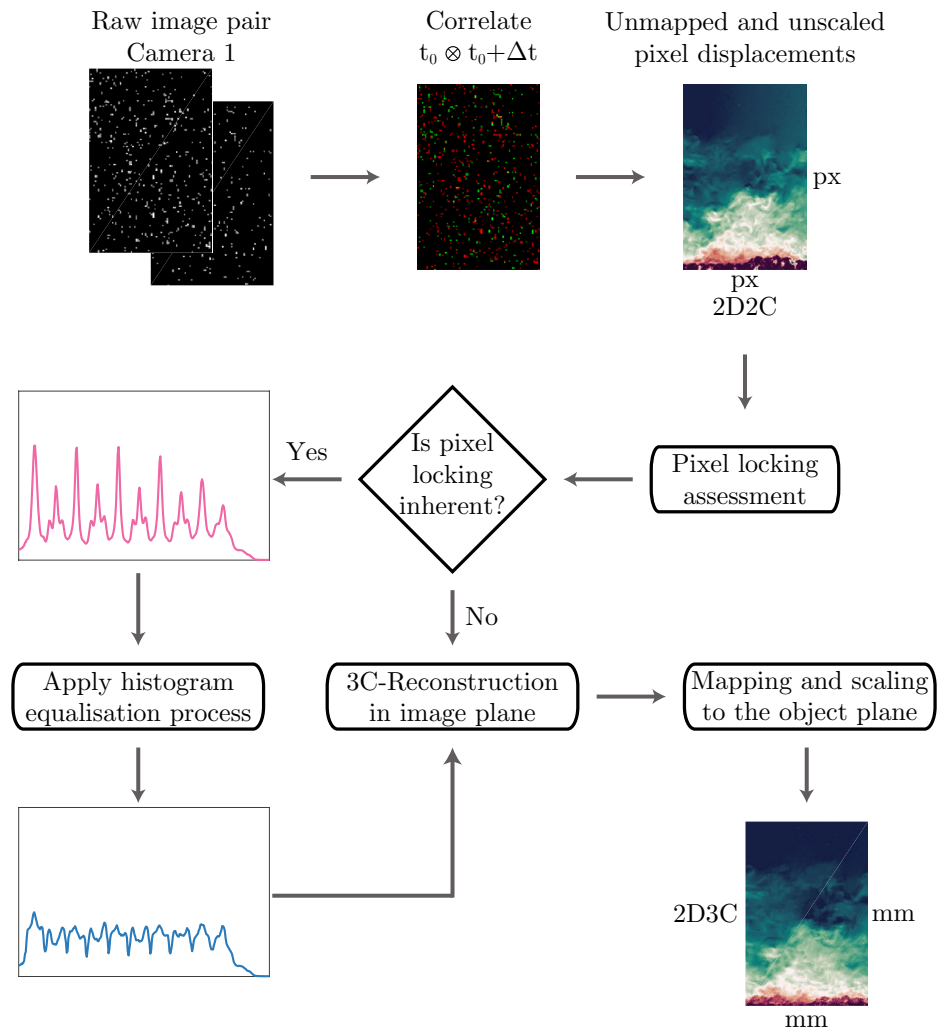


Fig. 2 Illustration of the influence of pixel locking on single point statistics following computation of 2D3C vector field in the object plane for an experimentally obtained zero-pressure gradient turbulent boundary layer (Case A) and its absolute pixel-locked variant (Case

B). **a** Histogram of the displacement component in the x -direction for the left camera, **b** mean profile of the streamwise velocity component, u , **c** RMS profile of the streamwise velocity component, u_{rms}

Fig. 3 Flowchart of the proposed strategy to correct for pixel locking per camera image in SPIV. Colouring of the particles in the correlation process has no physical meaning and is purely for clarity between the first and second frame. Correction is applied only if the frame is contaminated with pixel locking prior to reconstruction of the 2D3C vector fields



$$X_{\text{right}} = f_3(x, y, z), \quad (5)$$

$$Y_{\text{right}} = f_4(x, y, z), \quad (6)$$

where $(X_{\text{left}}, Y_{\text{left}})$ and $(X_{\text{right}}, Y_{\text{right}})$ are the corresponding positions in the image plane of the marker positions (x, y, z) in the object plane for the left and right cameras respectively. The mapping function is a third order polynomial in the spanwise, x , and wall-normal, y , direction and is linear for the streamwise component, z .

The second step comprises establishing the common reconstruction region when projected in both the left and the right camera. This allows a new grid to be generated upon which the data is interpolated. The derivatives of the mapping functions, w.r.t x , y and z , are then calculated at each point in the new grid. For the given particle image displacement ΔX_{left} , ΔY_{left} , ΔX_{right} and ΔY_{right} , the fluidic displacements dx_f , dy_f and dz_f , are found by inversion of the

mapping function derivatives matrix and performing a non-linear least squares fitting algorithm, as shown in Eq. (7).

$$\begin{bmatrix} \Delta X_{\text{left}} \\ \Delta Y_{\text{left}} \\ \Delta X_{\text{right}} \\ \Delta Y_{\text{right}} \end{bmatrix} = \begin{bmatrix} \frac{df_1}{dx} & \frac{df_1}{dy} & \frac{df_1}{dz} \\ \frac{df_2}{dx} & \frac{df_2}{dy} & \frac{df_2}{dz} \\ \frac{df_3}{dx} & \frac{df_3}{dy} & \frac{df_3}{dz} \\ \frac{df_4}{dx} & \frac{df_4}{dy} & \frac{df_4}{dz} \end{bmatrix} \cdot \begin{bmatrix} dx_f \\ dy_f \\ dz_f \end{bmatrix} \quad (7)$$

Prior to implementation, it is important to gauge the effectiveness of the in-house SPIV reconstruction script. A shear profile with known pixel displacement was applied to synthetically generated particles, under no influence of pixel locking. The resultant images were processed and velocity field reconstruction was carried out through both image plane-based and object plane-based methods. Comparison of the true mean velocity field with the results of the two cross-correlation techniques shows good agreement with an RMS deviation in the streamwise velocity corresponding to $\pm 0.32\%$ and $\pm 0.71\%$ of the freestream velocity for image

plane-based and object plane-based reconstruction respectively. Such a small difference in the RMS error offers a high degree of confidence in the image plane reconstruction technique and based on the above analysis, the robustness of the in-house script can be endorsed, with similar accuracy expected for diverse or more complex flows.

5 Pixel-locking correction

The predefined methodology was first applied and tested on synthetically generated data. A script capable of generating synthetic SPIV images was devised. Although devoid of aspects such as optical distortions, the use of synthetic images transcends the experimental limitations and allows the study of extreme pixel-locked conditions in SPIV. The synthetic image generator is based on the pinhole camera model and the concept of isomorphism of projective space. The particles are described by a 2D Gaussian shape and are randomly distributed in space. Similarly, the laser sheet has a Gaussian profile and a thickness of roughly 1 mm in the object plane. The particles are subjected to a shear flow in the streamwise direction while the mean spanwise and wall-normal velocity are kept at zero. Snapshots are recorded with a specified time delay, Δt , between the frames. Following Petracci et al. (2004), the density of particles is maintained at 40 ppm mm^3 as at this value, the fraction of spurious vectors is zero and any loss in correlation is kept at a minimum. To closely replicate experimental data, the angle between the lens plane and the normal of the light sheet is kept at 35° for a cross-stream SPIV configuration. Further, to replicate turbulent properties of the flow, a turbulent intensity of 2.5% was applied to all 3 directions, viz., the streamwise, spanwise and wall-normal velocities.

The particle image diameter, d_p , is varied so as to model extreme, moderate, mild and no pixel locking scenarios. The same methodology as described in Sect. 2 is executed, with histogram equalisation applied only to Cases 1A, 1B and 1C. Comparison of the resulting flow statistics assesses the performance of each implemented technique and provides preliminary insight into the viability of the proposed

Table 2 Synthetic SPIV test cases

	Left camera	Right camera	$T.I_\infty$ (%)
Case 1A	1.0	1.0	2.5
Case 1B	1.5	1.5	2.5
Case 1C	2.0	2.0	2.5
Case 1D	3.0	3.0	2.5

The mean particle diameter, \bar{d}_p , was varied while the same turbulent intensity value was applied in all test cases

pixel-locking correction method in SPIV. Figure 6a, b exhibit consistency in the mean velocity profile for the spanwise, w and in-plane streamwise, u , velocity components. Irrespective of the level of pixel locking or the reconstruction technique used, the mean profile is conserved in all cases. Note that the wall-normal velocity component, v , is omitted to avoid redundancy since the same mean particle displacement and turbulent intensity were applied as for the spanwise velocity component, w and the same trend was observed.

The variation of the RMS with the wall-normal position is also considered for the spanwise velocity component, w

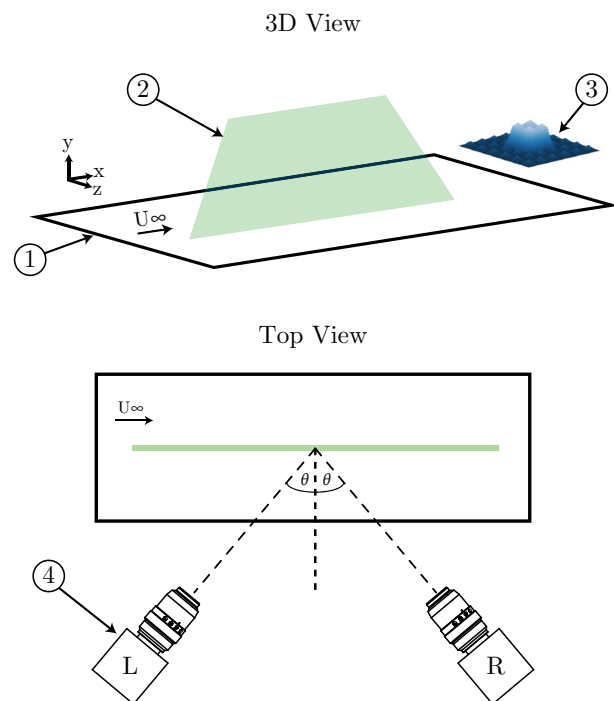
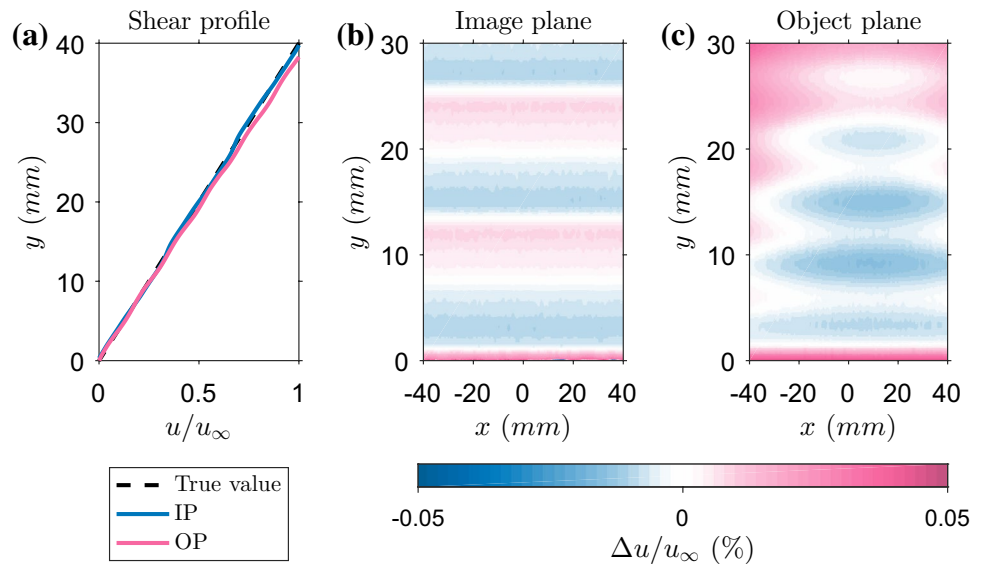


Fig. 4 This work follows the convention that x , y and z are the streamwise, wall-normal and spanwise directions with U , V and W being the corresponding velocities in those directions. U_∞ is the freestream velocity while θ is the angle between the lens plane and the normal of the laser sheet. (1. Wind tunnel floor 2. Laser sheet 3. Repeatable roughness element 4. Lavision Imager pro LX 16 MP cameras with L denoting the left camera and R denoting the right camera)

Table 1 Relevant parameters for the cameras used in the experiment

Sensor	KAI-16000 CCD
Resolution	4872 × 3248 pixels
Pixel size	7.4 μm
Aspect ratio	3:2
Fill factor	50%
f -stop	8.0
focal length	300 mm
Δt	46 μs

Fig. 5 A comparison between image plane-based reconstruction (IP) and object plane-based reconstruction (OP) is made to determine each method's accuracy. **a** The profile of the flow applied to the synthetic images is shown, together with a spatial averaging of velocity field for both the image and object plane-based reconstruction. Difference in velocity field between the true value and **b** image plane reconstruction and, **c** object plane reconstruction, expressed as a % of the freestream velocity



(Fig. 6c–e), and the in-plane streamwise velocity component, u (Fig. 6f–h). The severe overestimation of the RMS velocities for the extreme pixel locking case (Case 1A) can be attributed to sub-pixel displacements rounding towards integer values, thus resulting in discontinuities in u' , v' and w' . It is common knowledge that an increase in d_τ leads to a mitigation in the pixel-locking bias and it is evident from Fig. 6 that the discrepancy of the RMS velocities in comparison to the true value follows a similar trend.

It is compelling to note the disparity between the RMS velocities computed through object plane-based cross-correlation and the true value. In fact, in the presence of pixel locking, image plane-based reconstruction methodology results in 15–22% more accurate results. Furthermore, application of histogram equalisation to the pixel-locked cases brings an additional improvement of 5%. Such a trend can be observed in Fig. 7, where the difference between the true RMS and the computed RMS from the image plane methodology converges towards zero as d_τ increases. Although, application of the proposed protocol leads to improved flow statistics, there still exists limitations in extreme pixel-locking scenarios such as Case 1A where it is not viable to retrieve the data lost due to the sub-pixel displacement not being sufficiently resolved. Nevertheless, these findings demonstrate the superior attributes of image plane-based 2D3C reconstruction in tackling the interpolation part of the pixel-locking bias.

6 Validation study

In order to endorse and validate the method applied in the previous section, a range of experimental test cases was considered. Datasets for 3 different combinations of the

mean particle image diameter per camera corresponding to distinct scenarios of pixel locking are obtained by slightly defocusing the lens (Table 3). Each camera recorded 1250 image pairs ensuring convergence of statistics is reached. The image particle diameter was determined using the width of the autocorrelation peak of the pixels and finding where the intensity reaches half of its value.

An initial assessment of the severity of pixel locking in each case is performed by computing histograms of the sub-pixel displacement. Since pixel locking is not biased towards any particular direction, the streamwise and wall-normal pixel displacements are combined in the histograms (Hearst and Ganapathisubramani 2015). In the event of pixel locking, a peak is expected at a sub-pixel value of zero since the pixel displacements remain locked onto integer values. Application of histogram equalisation reorganises the initial histogram and reduces the bias contaminating the pixel displacements. Corrections are only applied on pixel-locked points in order to avoid distorting any flow features which are not influenced by this bias error. As observed in Fig. 8, Case 2A exhibits clear symptoms of pixel locking since \bar{d}_τ in each camera is less than the threshold value of 2 px. Histogram equalisation reduces the intensity of the peak and renders the distribution more uniform. The fact that the corrected histogram of Case 2A closely matches Case 2C, which is representative of a dataset devoid of pixel locking, implies that the presence of a less intense peak in the histogram can be attributed to flow phenomenology rather than pixel-locking effects. This is of significant importance as it shows that pixel-locking corrections can be performed on individual camera images separately and flow features can be recovered and preserved.

Following reconstruction of the velocity field, a comparison of the mean and fluctuating statistics is carried out

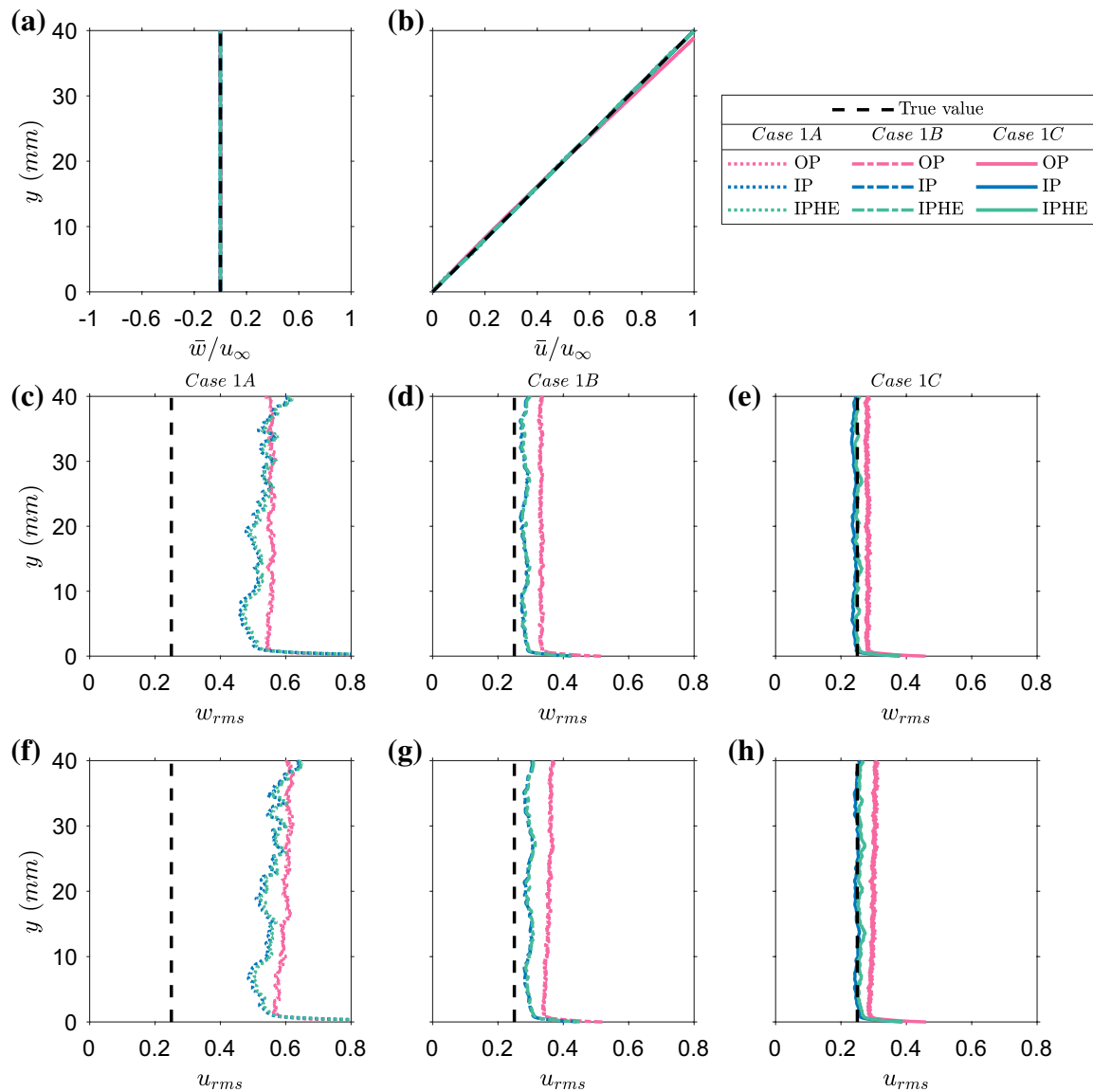


Fig. 6 Single-point statistics for synthetically generated datasets. **a** Mean spanwise, w , velocity profile normalised by the maximum streamwise velocity, u_∞ . **b** Mean streamwise, u , velocity profile normalised by the maximum streamwise velocity, u_∞ . **c–e** Spanwise RMS velocity, w_{rms} , variation with height for Cases 1A, 1B and 1C

respectively. **f–h** Streamwise RMS velocity, u_{rms} , variation with height for Cases 1A, 1B and 1C respectively. Note that the black dotted line in all the plots shows the actual value applied to the synthetic images

(Fig. 9). Concordant with the observations of Christensen (2004), the mean streamwise velocity profile remains uninfluenced by either the pixel-locking bias or the methodology used for the 2D3C reconstruction (Fig. 9a). The turbulent intensity (T.I), a function of the RMS of the streamwise velocity component, shows a variation of up to 3% between Case 2A and Case 2C while histogram equalisation produces an improvement of the order of less than 1%. Such minimal

improvement in the turbulent intensity can be attributed to the low level of pixel locking in the experimental dataset as can be observed in Fig. 8. However, it is interesting to note the impact of using image plane cross-correlation. The latter acts as a filter to adjust the interpolation part of the pixel-locked bias, resulting in improved flow statistics.

A unique case arises when only one camera in a SPIV configuration experiences pixel locking (Case 2B). The

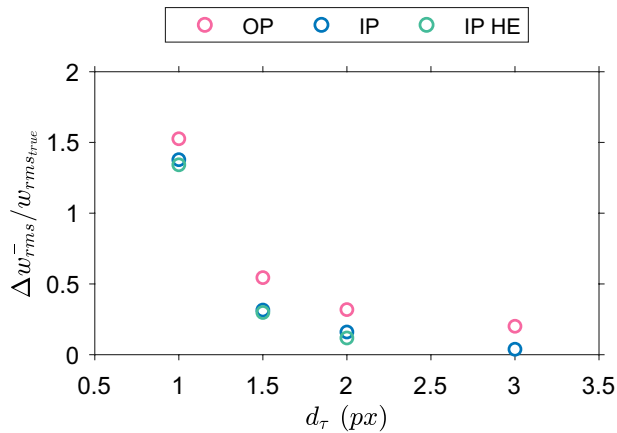


Fig. 7 Variation of the difference in RMS between the true value and the derived value from diverse adopted methodologies as the particle image diameter, d_τ , increases

Table 3 Experimental SPIV test cases with the specified mean particle diameter, \bar{d}_τ , for each camera

	Case 2A	Case 2B	Case 2C
Left camera	1.2	1.2	2.0
Right camera	1.2	2.0	2.0

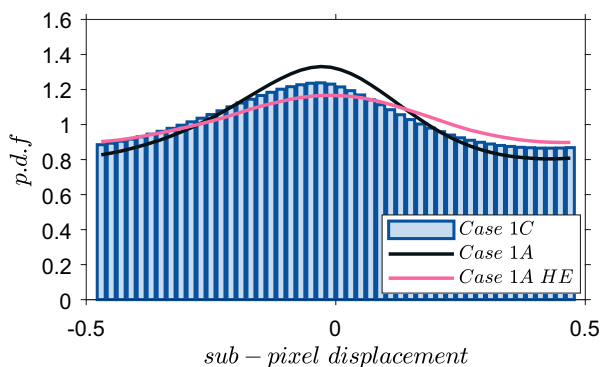


Fig. 8 Histogram of the sub-pixel displacement for Case 2C (blue-shaded region) representative of a non-pixel-locked case, Case 2A (black line) which represents pixel-locked data and Case 2A post histogram-equalisation (pink line). Only left-camera data is shown to avoid redundancy. The p.d.f represents the number of counts normalised by the area of the histogram

advantage of image plane cross-correlation is further emphasised in such a situation as this approach allows application of histogram equalisation to the contaminated pixel displacements in one camera only prior to reconstruction of the 2D3C velocity fields. Congruent with previous observations, Fig. 10a confirms no meaningful variation in the mean statistics of the streamwise velocity. However, the histogram equalised turbulent intensity

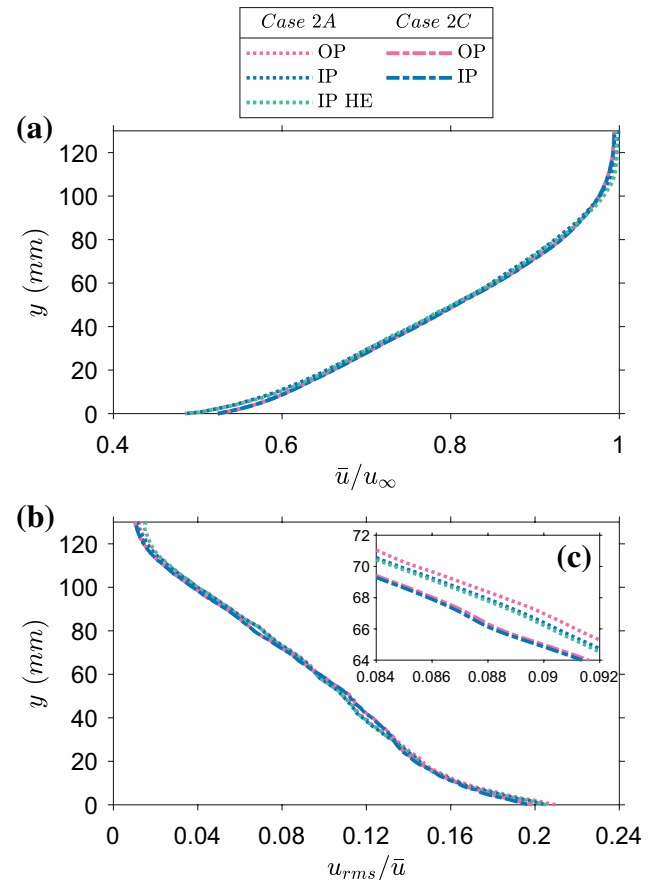


Fig. 9 Comparison between the single-point flow statistics of Case 2C and Case 2A pre- and post-histogram equalisation. **a** Plot of the streamwise mean velocity profile, **b** plot of the turbulent intensity profile in the streamwise direction and **c** a zoomed-in plot of the turbulent intensity profile to distinguish between the applied methodologies. *OP* object plane cross-correlation, *IP* image plane cross-correlation, *IP HE* image plane cross-correlation post histogram equalisation)

offers a 1.61% improvement (Fig. 10c). The ability to ameliorate the accuracy of the flow statistics highlights the diverse nature of the proposed protocol to deal with contrasting datasets corrupted by pixel locking.

7 Moiré fringes correction

In this section, we consider a cross-stream SPIV dataset for a variant of the multi-scale roughness element used in Sect. 6. Instantaneous processed vector fields are found to be devoid of such fringes as the variations in the flow overwhelms the aberrations arising from Moiré fringes. Rather, the fringes emerge in the mean flow statistics irrespective of the velocity component analysed. Ideally, a sensor with a fill factor of 100% would not be influenced by Moiré patterns but in practice, this is not achievable due

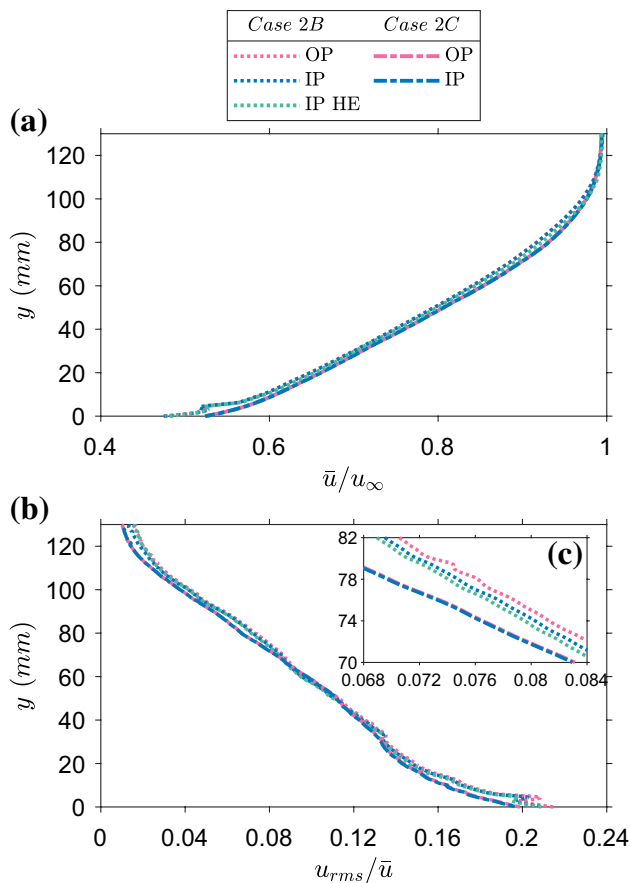


Fig. 10 Comparison between the single-point flow statistics of Case 2C and Case 2B pre- and post-histogram equalisation. **a** Plot of the streamwise mean velocity profile, **b** plot of the turbulent intensity profile in the streamwise direction and **c** a zoomed-in plot of the turbulent intensity profile to distinguish between the applied methodologies

to physical limitations of the camera. Alternatively, there exists techniques such as Gaussian blurring, “descreening” algorithms or “despeckle” processes which provide significant attenuation (Wen and Khatibi 2015). However, the trade-off of using these is a reduction in sharpness or brightness of the image. It has been shown that moving the sensor array mechanically can also help. Unfortunately, such jittery motion is not applicable in the context of PIV where calibration of the images is a crucial step in determination of the velocity fields. Hence, targeting the cross-correlation method and improving the residual of the interpolation method remain the most convenient method to tackle Moiré fringes.

For example, Fig. 11 shows the reconstructed mean velocity component of SPIV measurements following subtraction of a moving mean which was calculated using a sliding window with a length 25% the size of the velocity field. From Fig. 11a, it can be observed that object plane-based cross-correlation still contains Moiré fringes as the interference error progresses

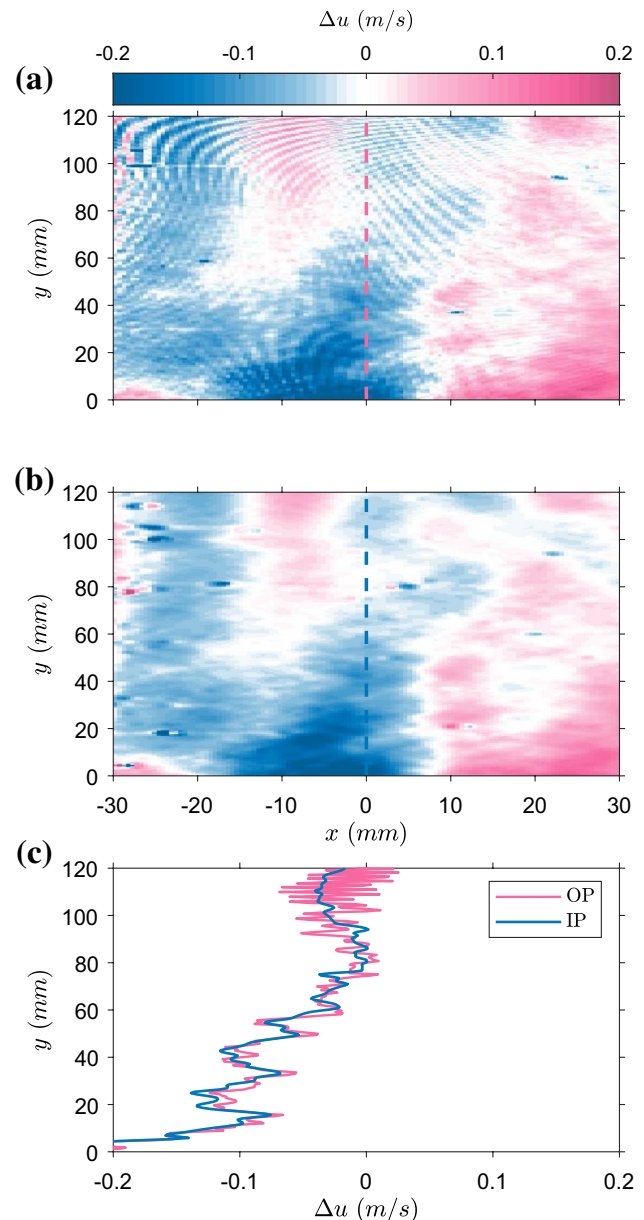


Fig. 11 Contour plot of the mean in-plane velocity component following subtraction of a moving mean window for **a** object plane-based cross-correlation, **b** image plane-based cross-correlation, **c** variation of the mean in-plane velocity component profile at the location $x = 0$, which exposes the high frequency artifacts present in **a**

into the object plane during the dewarping stage of the raw images. Paradoxically, performing cross-correlation in the image plane results in the removal of any potential fringes because the smoothing nature of such a process acts as a filter against such high frequency imaging artifacts. Moiré fringes is a common problem encountered in SPIV which goes unreported and can have negative influence on the mean statistics. Figure 11c illustrates the high frequency features of the fringes which can be detected as high amplitude fluctuations in the reconstructed mean velocity field. It is critical to remove

such artifacts as this leads to higher precision in the velocity field reconstruction. Image plane cross-correlation thus represents an alternative method to adopt in order to filter out Moiré fringes which, in comparison to blurring algorithms or mechanical motion of the sensor, maintains the high quality of both the image and the calibration.

8 Summary

An investigation was carried out to assess the accuracy of two distinct approaches for cross-correlation in SPIV when subjected to the influence of pixel locking. This direct comparison involved the use of a commercial software, which adopts an object plane-based cross-correlation technique, and an in-house SPIV reconstruction script, representative of the image plane alternative. A blueprint was devised to address pixel-locking bias via application of histogram equalisation post cross-correlation in the image plane prior to reconstruction of the 2D3C velocity field. The proposed strategy was tested on synthetically generated SPIV images and validated using experimental data.

Analysis of the flow statistics culminates in the following major findings:

- Object plane-based cross-correlation results in an overestimation of the turbulent statistics of the flow while image plane-based cross-correlation method contributes up to a 22% improvement in accuracy of the RMS velocities in the extreme pixel-locked scenario. Application of histogram equalisation under such conditions led to a further enhancement of 5%.
- Consistent with literature, it is observed that pixel-locking influence on the RMS reduces with an increase in particle image diameter while the mean remains unaffected. The difference between the computed RMS and the true value converges to zero as the particle diameter increases for image plane-based method while there still exists a certain offset for object plane-based method, thus highlighting the underlying erratum associated with such a technique.
- An additional disparity between the two approaches for cross-correlation is observed with the presence of Moiré fringes in the mean statistics. Contrary to object plane cross-correlation, the low pass filtering characteristics of image plane cross-correlation remove these high frequency artifacts and retrieve the appropriate mean velocity profile.

It can be concluded that although the loss in sub-pixel information due to pixel locking cannot be fully recovered, the accuracy of turbulent statistics can yet experience an improvement by adopting an adequate pixel-locking

correction technique coupled with image plane cross-correlation. Finally, the ability to simultaneously filter out high frequency artifacts in the mean velocities and deal with pixel-locking contamination in the RMS velocities advocates for a pervasive application of image plane cross-correlation in SPIV.

Acknowledgements This project was funded by the Engineering and Physical Sciences Research Council (EPSRC Grant No. EP/L006383/1). The authors are grateful to Mr Manuel A. Ferreira for his help in acquiring the experimental data in Sect. 5 and Dr Eduardo Rodriguez-Lopez for testing and debugging the in-house SPIV reconstruction script and for insightful conversations about Moiré fringes.

Open Access This article is licensed under a Creative Commons Attribution 4.0 International License, which permits use, sharing, adaptation, distribution and reproduction in any medium or format, as long as you give appropriate credit to the original author(s) and the source, provide a link to the Creative Commons licence, and indicate if changes were made. The images or other third party material in this article are included in the article's Creative Commons licence, unless indicated otherwise in a credit line to the material. If material is not included in the article's Creative Commons licence and your intended use is not permitted by statutory regulation or exceeds the permitted use, you will need to obtain permission directly from the copyright holder. To view a copy of this licence, visit <http://creativecommons.org/licenses/by/4.0/>.

Appendix

All data supporting this study are openly available from the University of Southampton repository at <https://doi.org/10.5258/SOTON/D1256>. The in-house SPIV reconstruction software and the synthetic image generator can be accessed using the following link: <https://git.soton.ac.uk/bharath-lab/2d-3c-piv-tools.git>. Follow the download instructions to build and compile the software on your machine.

References

- Adrian RJ, Westerweel J (2011) Particle image velocimetry. Cambridge University Press, Cambridge
- Beresh SJ, Wagner JL, Smith BL (2016) Self-calibration performance in stereoscopic PIV acquired in a transonic wind tunnel. *Exp Fluids* 57(4):1–17. <https://doi.org/10.1007/s00348-016-2131-y>
- Chen J, Katz J (2005) Elimination of peak-locking error in PIV analysis using the correlation mapping method. *Meas Sci Technol* 16(8):1605–1618. <https://doi.org/10.1088/0957-0233/16/8/010>
- Christensen KT (2004) The influence of peak-locking errors on turbulence statistics computed from PIV ensembles. *Exp Fluids* 36(3):484–497. <https://doi.org/10.1007/s00348-003-0754-2>
- Fincham A, Delerce G (2000) Advanced optimization of correlation imaging velocimetry algorithms. *Exp Fluids* 29(7):S013–S022. <https://doi.org/10.1007/s003480070003>
- Fore LB (2010) Reduction of peak-locking errors produced by Gaussian sub-pixel interpolation in cross-correlation digital particle image

- velocimetry. *Meas Sci Technol*. <https://doi.org/10.1088/0957-0233/21/3/035402>
- Gui L, Wereley ST (2002) A correlation-based continuous window-shift technique to reduce the peak-locking effect in digital PIV image evaluation. *Exp Fluids* 32(4):506–517. <https://doi.org/10.1007/s00348-001-0396-1>
- Hearst RJ, Ganapathisubramani B (2015) Quantification and adjustment of pixel-locking in particle image velocimetry. *Exp Fluids* 56(10):191. <https://doi.org/10.1007/s00348-015-2062-z>
- Hutchins N, Hambleton WT, Marusic I (2005) Inclined cross-stream stereo particle image velocimetry measurements in turbulent boundary layers. *J Fluid Mech* 541(1):21. <https://doi.org/10.1017/S0022112005005872>
- Kislava A, Sciacchitano A (2018) Peak-locking error reduction by birefringent optical diffusers. *Meas Sci Technol*. <https://doi.org/10.1088/1361-6501/aa97f7>
- Kwon YS, Philip J, De Silva CM, Hutchins N, Monty JP (2014) The quiescent core of turbulent channel flow. *J Fluid Mech* 751:228–254. <https://doi.org/10.1017/jfm.2014.295>
- Lecordier B, Demare D, Vervisch LMJ, Réveillon J, Trinité M (2001) Estimation of the accuracy of PIV treatments for turbulent flow studies by direct numerical simulation of multiphase flow. *Meas Sci Technol* 12(9):1382–1391. <https://doi.org/10.1088/0957-0233/12/9/302>
- Michaelis D, Neal DR, Wieneke B (2016) Peak-locking reduction for particle image velocimetry. *Meas Sci Technol* 27(10):104005. <https://doi.org/10.1088/0957-0233/27/10/104005>
- Nogueira J, Lecuona A, Nauri S, Legrand M, Rodríguez PA (2009) Multiple Δt strategy for particle image velocimetry (PIV) error correction, applied to a hot propulsive jet. *Meas Sci Technol*. <https://doi.org/10.1088/0957-0233/20/7/074001>
- Overmars E, Warncke N, Poelma C, Westerweel J (2010) Bias errors in PIV: the pixel locking effect revisited. 15th Int. Symp. Appl. Laser Tech. to Fluid Mech, Lisbon, Portugal, pp 5–8
- Petracci A, van Doorne CWH, Westerweel J, Lecordier B (2004) Analysis of Stereoscopic PIV Measurements using Synthetic PIV Images. In: Part. Image Velocim. Recent Improv., 2003. Springer, Berlin, pp 199–210. https://doi.org/10.1007/978-3-642-18795-7_14
- Raffel M, Willert CE, Wereley ST, Kompenhans J (2007) Particle image velocimetry. *Exp Fluid Mech*. <https://doi.org/10.1007/978-3-540-72308-0>
- Roesgen T (2003) Optimal subpixel interpolation in particle image velocimetry. *Exp Fluids* 35(3):252–256. <https://doi.org/10.1007/s00348-003-0627-8>
- Roth GI, Katz J (2001) Five techniques for increasing the speed and accuracy of PIV interrogation. *Meas Sci Technol* 12(3):238–245. <https://doi.org/10.1088/0957-0233/12/3/302>
- Shimizu M, Okutomi M (2002) Precise subpixel estimation on area-based matching. *Syst Comput Jpn* 33(7):1–10. <https://doi.org/10.1002/scj.10098>
- Soloff SM, Adrian RJ, Liu ZC (1997) Distortion compensation for generalized stereoscopic particle image velocimetry. *Meas Sci Technol* 8(12):1441–1454. <https://doi.org/10.1088/0957-0233/8/12/008>
- Stein AN, Huertas A, Matthies L (2006) Attenuating stereo pixel-locking via affine window adaptation. *Proc IEEE Int Conf Robot Autom* 2006(May):914–921. <https://doi.org/10.1109/ROBOT.2006.1641826>
- Wen W, Khatibi S (2015) Novel software-based method to widen dynamic range of CCD sensor images. In: Zhang YJ (ed) Lecture notes in computer science. Lect. Notes Comput. Sci. (including Subser. Lect. Notes Artif. Intell. Lect. Notes Bioinformatics), vol 9218. Springer International Publishing, Cham, pp 572–583. https://doi.org/10.1007/978-3-319-21963-9_53
- Westerweel J (1997) Fundamentals of digital particle image velocimetry. *Meas Sci Technol* 8(12):1379–1392. <https://doi.org/10.1088/0957-0233/8/12/002>

Publisher's Note Springer Nature remains neutral with regard to jurisdictional claims in published maps and institutional affiliations.